From Tb_3Ni_2 to Tb_3CoNi: The interplay between chemistry, structure, and magnetism

Clemens Ritter,[1] Alessia Provino,[2,3,4] Francois Fauth,[5] Sudesh K. Dhar,[6] Vitalij K. Pecharsky,[3,7] and Pietro Manfrinetti[2,3,4,*]

[1]*Institut Laue-Langevin, BP 156, 38042 Grenoble, France*

[2]*Department of Chemistry, University of Genova, Via Dodecaneso 31, 16146 Genova, Italy*

[3]*The Ames Laboratory, US Department of Energy, Iowa State University, Ames, Iowa 50011, USA*

[4]*Institute SPIN-CNR, Corso Perrone 24, 16152 Genova, Italy*

[5]*CELLS-ALBA Synchrotron, Carrer de la Llum 2-26, 08290 Cerdanyola del Vallès, Barcelona, Spain*

[6]*Department of Condensed Matter Physics and Materials Science, Tata Institute of Fundamental Research, Homi Bhabha Road, Mumbai 400 005, India*

[7]*Department of Materials Science and Engineering, Iowa State University, Ames, Iowa 50011, USA*

(Received 13 December 2018; revised manuscript received 25 January 2019; published 20 February 2019)

Formation, crystal structure, and macroscopic and microscopic magnetism of the binary Tb_3Ni_2 and derivative pseudobinary $Tb_3Co_xNi_{2-x}$ phases have been investigated using an array of experimental methods. While Tb_3Ni_2 crystallizes in the monoclinic Dy_3Ni_2 structure type (*mS*20, *C*2/*m*), the substitution of Co for Ni results in a structural transition into the rhombohedral Er_3Ni_2 type (*hR*45, $R\bar{3}h$) at $x(\mathrm{Co}) \approx 0.34$ and beyond in the $Tb_3Co_xNi_{2-x}$ system. In both the monoclinic and rhombohedral phases, the addition of Co leads to an anisotropic change of lattice parameters and unexpected reduction of the cell volume. Measurements of bulk properties reveal that these compounds order ferrimagnetically or ferromagnetically at about 100 K. Complex noncollinear ferromagnetic ordering in the Tb sublattices is weakly dependent on composition. For $x > 0.34$ the long-range magnetic ordering leads to a strong anisotropic magnetostriction accompanied by a symmetry reduction from rhombohedral to triclinic.

DOI: 10.1103/PhysRevMaterials.3.024406

I. INTRODUCTION

Design and discovery of innovative materials, capable of meeting the rapidly growing demand for renewable energy, remain among the main objectives for materials science, chemistry, and physics. With this in mind, rare-earth (*R*) based compounds are noteworthy because they demonstrate fundamental phenomena of practical significance [1–3]. Alloys, ceramics, glasses, and inorganic, organometallic, and hybrid materials that contain rare earths are routinely used in consumer products. Scandium, yttrium, and many of the lanthanides are found in both hybrid and electric vehicles, smart phones and tablets, computer monitors and hard drives, rechargeable nickel-metal-hydride batteries, and light-emitting diodes. The importance of intermetallic compounds arises from a great variety of crystal structures supported by nearly limitless possibilities to combine rare earths with other metals and metalloids. This, in turn, creates conditions ripe for critical physical properties to emerge, especially considering that changing even a single $4f$ electron may introduce drastic differences in the chemistry and physics, like remarkable changes in structure and magnetism of *R*MgSn [4], *R*ScSb [5], and $R_{11}Ni_4In_9$ [6,7] when one *R* atom is replaced by another.

Stoichiometric binary R_3Ni_2 phases exist with $R =$ Y and Gd through Er [8,9]. Tb_3Ni_2 and Dy_3Ni_2 adopt the monoclinic Dy_3Ni_2 type (*mS*20, *C*2/*m*) [10], while rhombohedral Er_3Ni_2 (*hR*45, $R\bar{3}h$) [11] and tetragonal Y_3Ni_2 (*tP*80, $P4_12_12$) [12] crystallize in their own prototypes. Ho_3Ni_2 is dimorphic, the high-temperature form crystallizing with the Dy_3Ni_2 type and the low-temperature form adopting the Er_3Ni_2 type [10]. Originally in doubt [9,13], Gd_3Ni_2 and derivative $Gd_3Co_xNi_{2-x}$ crystallize in the Dy_3Ni_2 type, ordering ferromagnetically with Curie temperatures, T_C, ranging between 147 K (Gd_3Ni_2) and 175 K (Gd_3CoNi) [14,15]. Two successive magnetic transitions have been reported in Ho_3Ni_2 and Er_3Ni_2: the high-temperature second-order paramagnetic to ferromagnetic (FM) transitions, followed by possible spin reordering at low temperature [16]. Magnetism of Tb_3Ni_2 has not been reported in the literature.

Since Tb_3Ni_2 remains the only known representative of the family without reported magnetic properties, we have reinvestigated its crystal structure and characterized its magnetic behaviors together with those of substituted $Tb_3Co_xNi_{2-x}$ derivatives. X-ray and neutron powder-diffraction data show that the replacement of Ni by Co in the parent Tb_3Ni_2 destabilizes the monoclinic Dy_3Ni_2 type, causing a transition to the rhombohedral Er_3Ni_2 type when $x(\mathrm{Co}) \geqslant 0.34$. Further, the magnetic transition in the rhombohedral phase is accompanied by a strong anisotropic magnetostriction and symmetry reduction from rhombohedral to triclinic. Here we report the interplay between the composition, crystal structure, and magnetism of the title materials derived from temperature-dependent and magnetic-field-dependent magnetization, specific heat, x-ray diffraction, and temperature-dependent neutron- and synchrotron-diffraction measurements.

*Corresponding author: chimfis@chimica.unige.it

II. RESULTS AND DISCUSSION

Sample preparation and other experimental details are found in the Supplemental Material (SM) [17]. Binary Tb_3Ni_2 and all of the pseudobinary $Tb_3Co_xNi_{2-x}$ phases form via peritectic reactions that occur at nearly constant temperatures, i.e., 1004 K for Tb_3Ni_2 (lower than 1104 K reported earlier [18,19]) and 995 K for Tb_3CoNi. Crystallographic differences that occur as x(Co) changes (see the next section) lead to distinctly different, i.e., platelike and equiaxed, grain morphologies that are, respectively, observed in the monoclinic and the rhombohedral phase regions as illustrated in scanning electron microscopy (SEM) microphotographs of representative samples [see Figs. S1(a)–S1(d) in SM [17]]. Small amounts of $TbNi_{1-x}Co_x$ are often present as an impurity phase. This minor impurity 1:1 phase is undetectable in x-ray-diffraction patterns, which is expected since, according to SEM, its presence is restricted to some small regions of the samples (not exceeding 2–3 vol. %). Overall concentration is likely less than 2 vol. %, which is on the edge of the sensitivity of the technique. Magnetic ordering of this impurity phase should, in principle, be visible in the low-temperature neutron data, as the magnetic peaks are expected to be strong due to the large Tb moment. However, we do not see any additional magnetic peaks at low temperatures (Sec. II B), pointing again to a very low overall concentration, i.e., beyond detection limits of this technique as well. Further, if this impurity phase was present, its magnetic peaks would not overlap with those of the $Tb_3Ni_{2-x}Co_x$ phase. Given this, the influence of the impurity detectable in SEM on the data treatment of the magnetic refinements of the main phase (Sec. II C) is negligible.

A. Crystal structure of Tb_3Ni_2 and $Tb_3Co_xNi_{2-x}$

Similar to Gd_3Ni_2, binary Tb_3Ni_2 crystallizes in the monoclinic Dy_3Ni_2 prototype [3]. However, introduction of Co alters the crystal structures of these two binary phases differently despite only a single $4f$-electron difference between Gd and Tb. In $Gd_3Co_xNi_{2-x}$, the Dy_3Ni_2 type is preserved up to x(Co) = 1.0; at higher x(Co), the compound adopts the orthorhombic Y_3Co_2 type [8]. In the $Tb_3Co_xNi_{2-x}$ series, on the other hand, a structural change from the monoclinic Dy_3Ni_2 to the rhombohedral Er_3Ni_2 type occurs at x(Co) $\cong$ 0.33, and this structure is preserved at least up to x(Co) = 1. The lattice parameters as functions of the Co content are shown in Fig. 1 and in Table SI in SM [17]. In the monoclinic phase a nearly linear reduction of both a and c is opposite to the nearly linear increase of b and β as the x(Co) increases. A small but abrupt anomaly is seen when x(Co) approaches 0.33. In the rhombohedral phase, a similar behavior is observed with a increasing and c falling nearly linearly, with anomalous behavior in the immediate vicinity of the phase transformation. The anisotropic change of lattice parameters gives rise to a progressive contraction of the unit-cell volume in both structures. In principle, the replacement of Ni by Co should lead to expansion of the unit cell regardless of structure, since the effective atomic volume of the elemental Co (11.08 Å^3) is slightly larger than that of Ni (10.93 Å^3) [20]. The opposite trend observed here may be attributed to the fact that Co assumes an anomalously large volume in its elemental form, while it behaves as a normal $3d$ metal with a smaller atomic volume than Ni when alloyed [21].

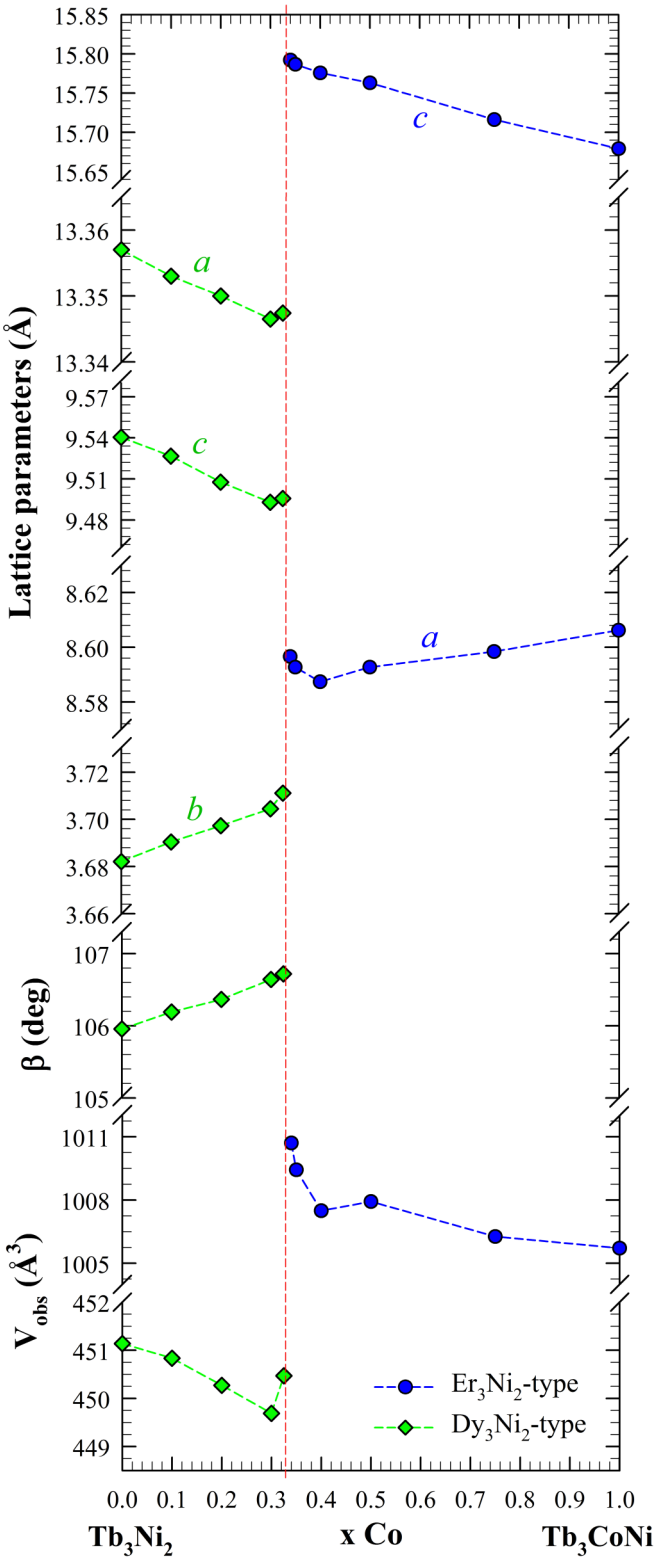

FIG. 1. Lattice parameters and unit-cell volumes as functions of x(Co) in the $Tb_3Co_xNi_{2-x}$ series.

Dy_3Ni_2 and Er_3Ni_2 prototypes are geometrically related to one other, and they are also related to the structures of the equiatomic CrB, FeB, and TbNi [10,15]. All of these structures are built from Ni-centered trigonal prisms formed by the rare-earth atoms [11]. In the binary monoclinic Tb_3Ni_2 (and $Tb_3Co_xNi_{2-x}$), three of the five inequivalent $4i$ sites are occupied by the Tb atom and two are occupied by the Ni atom (or a statistical mixture of Ni and Co atoms). In the rhombohedral $Tb_3Co_xNi_{2-x}$ three symmetry-inequivalent ($3a$, $6c$, and $18f$) sites are occupied by the Tb atoms, while another $18f$ site is filled by a mixture of Co and Ni atoms. Both types of structures are sketched in Fig. S2 in SM [17]. A gradual increase of x(Co) in $Tb_3Co_xNi_{2-x}$ causes a progressive change in the strengths and lengths of the R-Co/Ni bonds, which may be the main factor leading to the structural change at $x(\mathrm{Co}) \cong 0.33$. It is worth mentioning that a similar structural change occurs in Ho_3Ni_2, which is, however, dependent on the details of the synthesis: this compound adopts the Dy_3Ni_2 type when annealed below the melting point while the Er_3Ni_2 type is formed through rapid cooling [10].

B. Bulk magnetism of Tb_3Ni_2 and $Tb_3Co_xNi_{2-x}$

The temperature dependencies of the dc magnetization, $M(T)$, of Tb_3Ni_2, $Tb_3Co_{0.5}Ni_{1.5}$, and Tb_3CoNi measured in zero field-cooled (ZFC) and field-cooled (FC) modes are shown in Figs. 2(a)–2(c). The effective magnetic moments, μ_{eff}, derived from Curie-Weiss fits of the data above 200 K [see Figs. S3(a)–S3(c) in SM [17]] are 10.16, 10.28, and 10.11 μ_B/Tb^{3+} in Tb_3Ni_2, $Tb_3Co_{0.5}Ni_{1.5}$, and Tb_3CoNi, respectively; these values slightly exceed the theoretical Hund's rule-derived value of 9.72 μ_B for the noninteracting Tb^{3+} ion [22] and may indicate small moments on Ni/Co. Positive Weiss temperatures of 106, 96, and 98 K determined for Tb_3Ni_2, $Tb_3Co_{0.5}Ni_{1.5}$, and Tb_3CoNi, respectively, *prima facie* suggest ferromagnetic or ferrimagnetic (FIM) ground states.

The $M(T)$ behaviors of the rhombohedral $Tb_3Co_{0.5}Ni_{1.5}$ and Tb_3CoNi are similar. In both cases, low-field ZFC and FC data diverge, showing thermomagnetic irreversibility [Figs. 2(b) and 2(c), respectively]; typical of FIM or FM materials, the latter is observed over a progressively smaller temperature window as the measurement field increases. The isothermal magnetizations, $M(H)$, measured at 2 K for $Tb_3Co_{0.5}Ni_{1.5}$ [Fig. 3(a)] and at 4 and 75 K for Tb_3CoNi [Fig. 3(b)], are typical of FM and FIM compounds, with coercive fields H_C of 3.6 kOe at 2 K for $Tb_3Co_{0.5}Ni_{1.5}$ and 2.5 kOe for Tb_3CoNi at 4 K. These relatively large coercive fields explain the thermomagnetic irreversibilities in $M(T)$, especially when the applied fields are smaller than H_C.

The $M(T)$ and $M(H)$ behaviors for Tb_3Ni_2 [Figs. 2(a) and 4, respectively] show different features. The $M(H)$ data at 2 K show two field-induced metamagnetic transitions at $H_1 = 13$ kOe and $H_2 = 48$ kOe, with the magnetization nearly saturating at higher fields [Fig. 4(a)]; the metamagnetic transition at H_2 is preserved at 5, 10, and 30 K [Figs. 4(b)–4(d)]. The low-field ZFC and FC $M(T)$ data of Tb_3Ni_2 show no thermomagnetic irreversibility in contrast to the two other compounds. Clear peaks in $M(T)$, their shift toward low temperature [Fig. 2(a)], and low-temperature metamagnetism

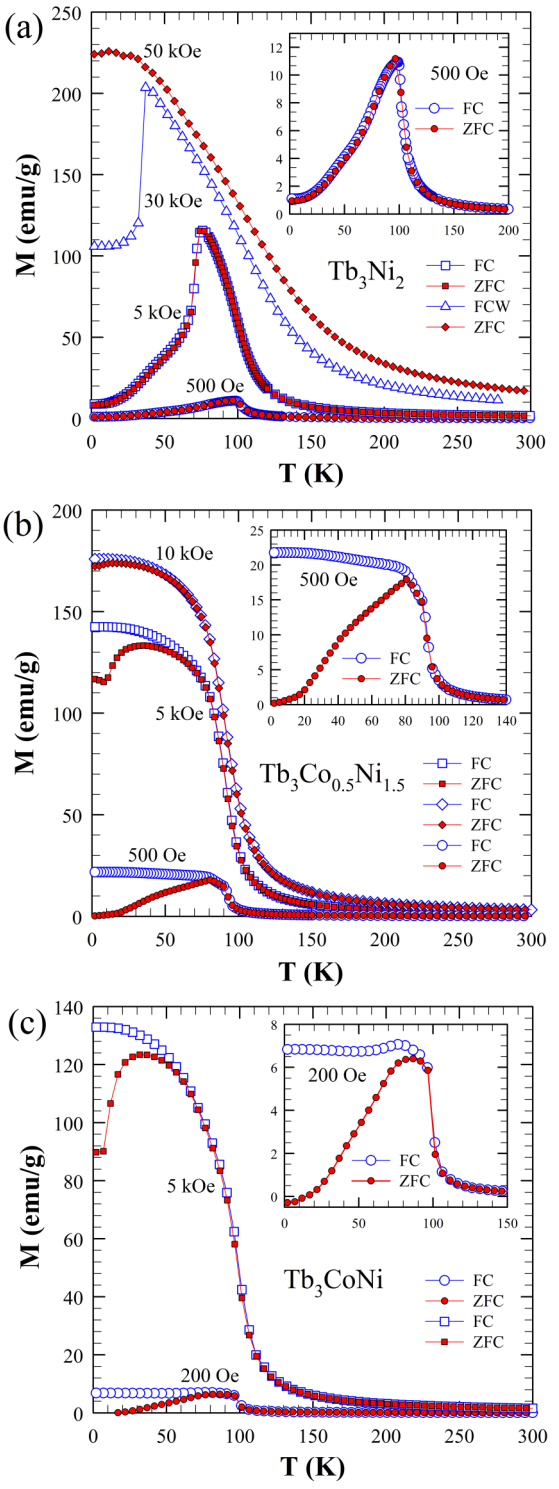

FIG. 2. (a) $M(T)$ of Tb_3Ni_2 measured between 2 and 300 K in 500-Oe and 5-, 30-, and 50-kOe magnetic fields; the inset clarifies 500-Oe data. (b) $M(T)$ of $Tb_3Co_{0.5}Ni_{1.5}$ measured between 2 and 300 K in 500-Oe and 5- and 10-kOe magnetic fields; the inset clarifies 500-Oe data. (c) $M(T)$ of Tb_3CoNi measured between 2 and 300 K in 200-Oe and 5-kOe magnetic fields; the inset clarifies 200-Oe data. Lines are guides for the eye.

[Fig. 4] are typical characteristics of antiferromagnets. The transition from the paramagnetic to a magnetically ordered state, as deduced from the rapid change of magnetization

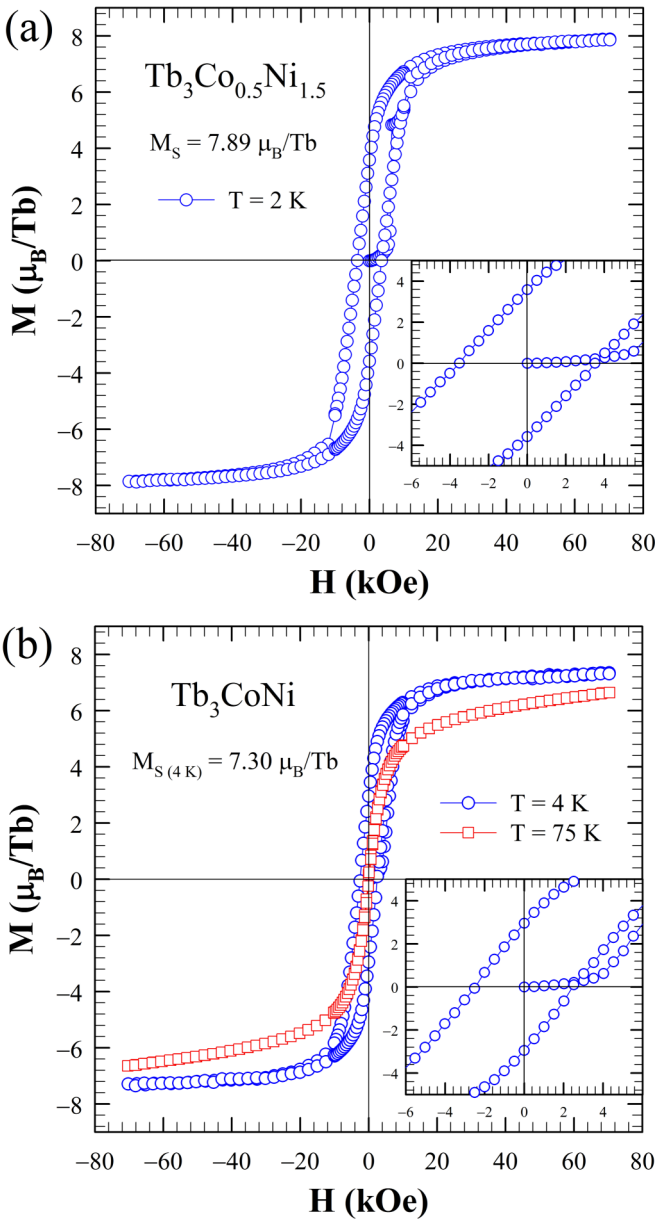

FIG. 3. (a) Isothermal magnetization of $Tb_3Co_{0.5}Ni_{1.5}$ measured at 2 K. (b) Isothermal magnetization of Tb_3CoNi measured at 4 and 75 K. The insets clarify low-field behavior.

around 100 K, on the other hand, broadens with increasing field, which is typical of either ferrimagnets or ferromagnets; $M(T)$ also shows saturation when measured at 50 kOe. The latter is in correspondence with the near saturation in the $M(H)$ plot at 2 K seen above 48 kOe. A coercive field of 1.8 kOe at 2 K is inferred from the $M(H)$ plot at that temperature [inset of Fig. 4(a)]. Lack of thermomagnetic irreversibility between the ZFC and FC $M(T)$ plots at 500 Oe is, therefore, surprising. Similarly, the absence of FM-like saturation of the FC $M(T)$ plots at 500 Oe and 5 and 30 kOe is also surprising and in contrast to the behavior observed in $Tb_3Co_{0.5}Ni_{1.5}$ and Tb_3CoNi.

Referring to the neutron-diffraction data discussed below, three independent Tb sublattices in all three compounds are FM, albeit not exactly collinear. Hence, the differences in $M(T)$ and $M(H)$ behaviors between representatives from the two different phase regions are quite likely related to the peculiar platelike microstructure of Tb_3Ni_2 [see Figs. S1(a) and S1(b) in SM [17]] and resulting strong preferred orientation in the bulk polycrystalline specimen employed in both $M(T)$ and $M(H)$ measurements. Random orientation of the magnetic field vector with respect to the highly textured polycrystalline sample coupled with very strong shape anisotropy of the platelets may, therefore, reflect (re)orientations of highly anisotropic strongly pinned domains in the direction of the magnetic field. Equiaxed grains and lack of preferred orientation [see Figs. S1(c) and S1(d) in SM [17]] explain why similar behavior is not seen in the other two compounds. Saturation magnetizations at 70 kOe are 8.1 μ_B/Tb for Tb_3Ni_2, 7.9 μ_B/Tb for $Tb_3Co_{0.5}Ni_{1.5}$, and 7.3 μ_B/Tb for Tb_3CoNi. All are lower than the expected 9 m_B/Tb. Principal parameters derived from bulk magnetization measurements are summarized in Table I. Minor contributions from Ni and, especially, Co cannot be completely excluded.

The heat capacities of Tb_3Ni_2 and Tb_3CoNi [see Figs. S4(a) and S4(b), respectively, in SM [17]] exhibit λ-type anomalies near 100 K reflecting single bulk magnetic transitions. The jump in the heat capacity of Tb_3CoNi is triple that of Tb_3Ni_2. The larger anomaly in the former compound can be attributed to the additional contribution from a structural distortion that occurs in Tb_3CoNi between 80 and 100 K as inferred from the neutron powder-diffraction data (see below) and also reflected as a broad specific-heat anomaly observed below the main peak. A simultaneous magnetic and structural transition will involve contributions from both the magnetic and configurational entropies, which is the primary reason for the giant magnetocaloric effects seen in compounds such as $Gd_5Si_2Ge_2$ [23] and $Tb_5Si_2Ge_2$ [24]. The smaller peak height in Tb_3Ni_2 can also be explained based on neutron-scattering data [see Fig. 8(f)] which show differing gradual increases of the magnetic moments on the three Tb sublattices in Tb_3Ni_2 below T_C. In the case of the Tb1 sublattice the saturation of the moment is attained only below 20 K. As a result, a smaller fraction of the total available magnetic entropy is released at T_C and hence a weaker jump in the heat capacity at T_C compared to that in Tb_3CoNi.

C. Neutron and synchrotron diffraction

Since the crystal structure of $Tb_3Co_xNi_{2-x}$ at room temperature changes at x(Co) ≅ 0.33, neutron- and synchrotron-diffraction experiments are discussed accordingly.

1. Compositions $0 \leqslant x(\mathrm{Co}) \leqslant 0.325$

Within this composition, the monoclinic Dy_3Ni_2-type structure (space group $C2/m$) remains stable. Figure S5 in SM displays the refinement of the synchrotron room-temperature data of $Tb_3Co_{0.30}Ni_{1.70}$, and Table SII in SM contains the results for the four compounds measured within this composition range either with synchrotron or with high angular resolution neutron powder diffraction [17]. Neither the atomic positions of the three Tb ions nor those of the two transition-metal sites change significantly in a systematic way as the limit of the stability of the $C2/m$ phase is approached.

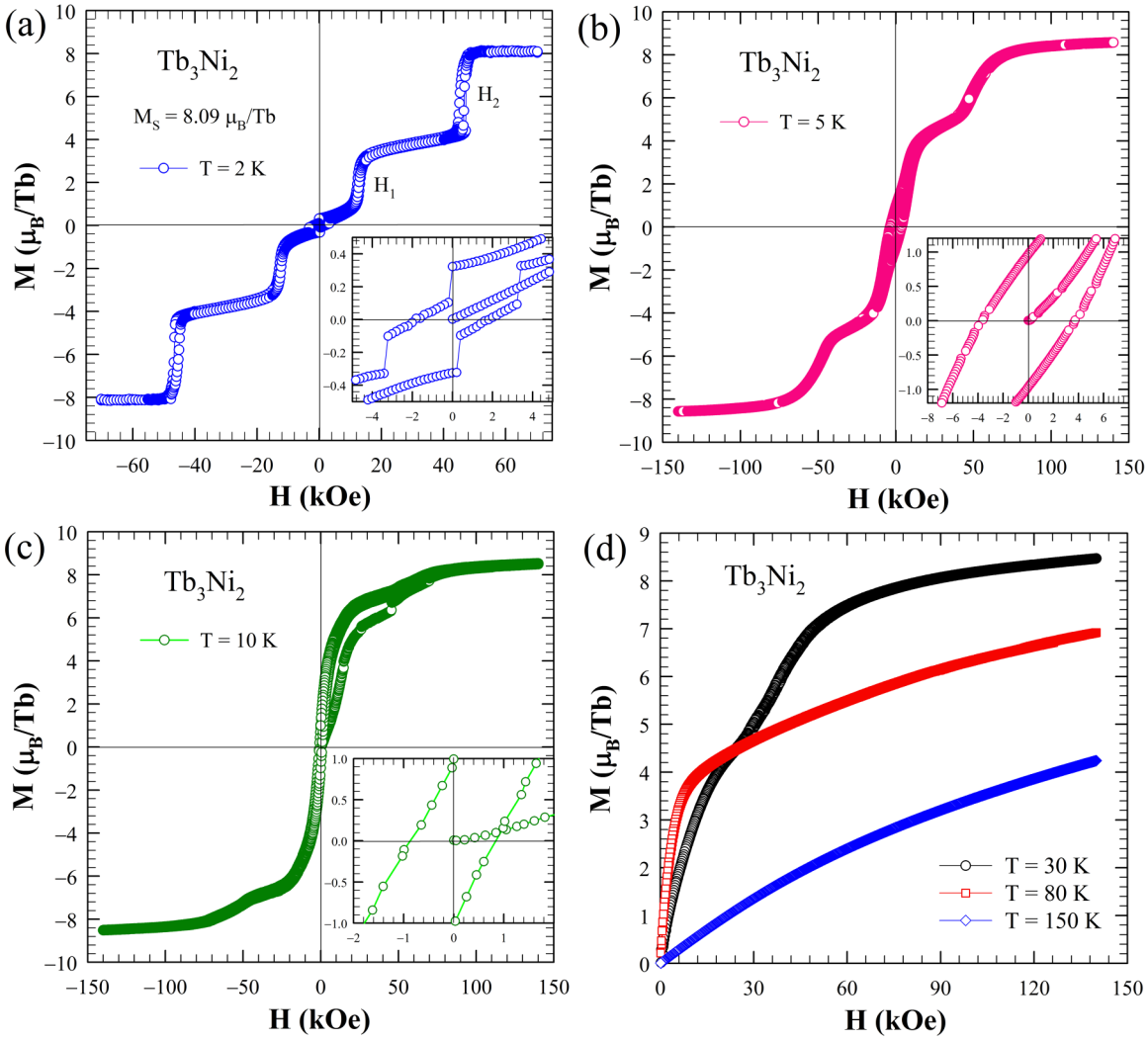

FIG. 4. Isothermal magnetization of Tb_3Ni_2 measured at 2 K (a), 5 K (b), 10 K (c), and 30, 80, and 150 K (d). The insets in (a)–(c) clarify low-field behavior.

On cooling, all compounds see a magnetic phase transition. Figure 5(a) exemplifies the low angle region of the thermodiffractogram of Tb_3Ni_2 (those of the other three compounds are similar). Below about 100 K an increase of several nuclear Bragg peaks is visible. This increase is not steady for all magnetic reflections: e.g., the first low angle reflection (001) decreases again below about 80 K, which can be linked either to a spin reorientation process or to a different temperature dependence of coexisting magnetic sites. As determined from integration of the magnetic peaks, the magnetic transition temperatures for all four compounds remain near 100 K, showing that x(Co) does not influence the onset of magnetic order. The magnetic propagation vector corresponds to $\kappa = 0$ and magnetic symmetry analysis was used to determine the allowed irreducible representations (IRs) and their basis vectors (BVs) for the Wyckoff site 4*i* in space group $C2/m$ (see Table SIII in SM [17]). Two of the allowed IRs contain BVs defining a ferromagnetic coupling while the two others defining an antiferromagnetic coupling between the magnetic ions. Only IR3 describing a ferromagnetic coupling in the direction of the *a*- and *c*-unit-cell vectors accounts for the magnetic intensity. The fact that all three Tb sublattices order at the same temperature with the same magnetic propagation vector and follow the same IR is worth highlighting. A totally different behavior was recently found in the two related series of rare-earth transition-metal compounds $R_5Ni_2In_4$ and

TABLE I. Magnetic parameters of Tb_3Ni_2, $Tb_3Co_{0.5}Ni_{1.5}$, and Tb_3CoNi compounds.

$Tb_3Co_xNi_{2-x}$	T_N/T_C (K)	μ_{eff} (μ_B/Tb^{3+})	θ_P (K)	H_C (kOe)	M_S (μ_B/Tb^{3+})
Tb_3Ni_2	95/100	10.16	106	1.8	8.09
$Tb_3Co_{0.5}Ni_{1.5}$	90	10.28	96	3.6	7.89
Tb_3CoNi	100	10.11	98	2.5	7.30

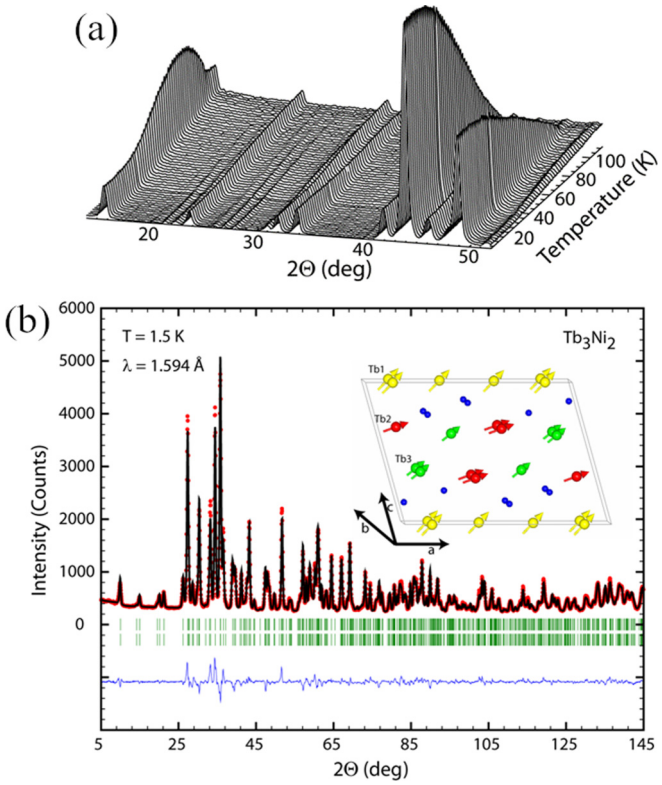

FIG. 5. (a) Low 2Θ part of the thermal dependence of the neutron-diffraction pattern of Tb_3Ni_2 between 1.5 and 112 K. (b) Rietveld refinement of the high angular resolution neutron powder data of Tb_3Ni_2 at 1.5 K. Observed (dots, red), calculated (black, line), and difference patterns are shown. The tick marks indicate the calculated position of the nuclear Bragg peaks. The inset shows the magnetic structure, and blue balls represent the transition-metal (Co/Ni) sites.

TABLE II. Results of the Rietveld refinements of the high angular resolution neutron powder-diffraction data at 1.5 K for $Tb_3Co_xNi_{2-x}$ in space group $C2/m$. All atoms are on Wyckoff position $4i$. C1 and C2 are the coefficients of the BV1 (100) and BV2 (001) of IR3. Atom coordinates for $x = 0.34$ were fixed to those of $x = 0.325$ (see Sec. III).

x	0	0.325	0.34
a (Å)	13.4012(4)	13.4083(4)	13.412(2)
b (Å)	3.6557(1)	3.6797(1)	3.6792(4)
c (Å)	9.4876(3)	9.4207(3)	9.413(1)
β (°)	105.873(2)	106.492(2)	106.55(1)
V (Å^3)	447.1	445.7	445.22
V_{at} (Å^3)	22.355	22.285	22.26
Tb1 x	0.1311(3)	0.1307(3)	
z	0.9984(3)	0.9983(3)	
C1	8.5(1)	8.7(1)	10.0(4)
C2	7.2(1)	6.4(1)	5.4(5)
μ_{Tb1} (μ_B)	9.5(2)	9.2(2)	9.9(8)
Tb2 x	0.4040(2)	0.4026(3)	
z	0.3259(3)	0.3254(3)	
C1	8.9(1)	9.2(1)	9.9(4)
C2	3.0(1)	2.8(1)	2.3(3)
μ_{Tb2} (μ_B)	8.6(2)	8.8(2)	9.5(6)
Tb3 x	0.1455(3)	0.1428(3)	
z	0.3717(3)	0.3712(3)	
C1	7.0(1)	7.3(1)	6.5(4)
C2	4.8(2)	5.1(1)	7.6(4)
μ_{Tb3} (μ_B)	7.4(2)	7.6(2)	8.5(7)
Co1/Ni1 x	0.5333(3)	0.5334(4)	
z	0.1443(4)	0.1459(5)	
Co2/Ni2 x	0.7430(3)	0.7433(4)	
z	0.2270(4)	0.2317(5)	
R_{Bragg}	6.2	6.3	4.8
R_{Mag}	7.5	7.4	4.6

$R_{11}Ni_4In_9$ (with R = Tb and Ho) [25] where separate ordering temperatures with different magnetic propagation vectors had been found for the different R sublattices. While the three Tb sites get magnetically long-range ordered, there is no sign of an ordered magnetic moment on the $3d$ metal sites. This magnetic structure is found for all four measured compounds in the range $0 \leqslant x < 0.325$.

Figure 5(b) displays the Rietveld refinement of the high angular resolution powder-diffraction data of Tb_3Ni_2 at 1.5 K. The magnetic structure is shown as an inset of the same figure; the magnetic space group is $C2'/m'$. Table II reports the results of the refinements of the 1.5-K high angular resolution neutron data of Tb_3Ni_2 and $Tb_3Co_{0.325}Ni_{1.675}$. Similar to room temperature (see Table SII in SM [17]), there are no significant differences in the structural details of Tb_3Ni_2 and $Tb_3Co_{0.325}Ni_{1.675}$ at 1.5 K. The values of the magnetic moments of the three Tb sites are as well nearly identical and therefore no indication can be discerned for the closeness to a radical structural change as found for $x > 0.34$ (see the next section).

The moment directions of the three Tb sites are determined by the ratio between the two coefficients C1 and C2 of the BVs (100 along the the a axis and 001 along the c axis). This ratio is not identical for the three sites and is, furthermore, changing as a function of temperature. Common to the three sites is the prevalence of the component pointing in the a direction and the existence of a positive c component. The moments are, however, not collinear as the angles adopted relative to a and c axes are different [inset of Fig. 5(b)].

A cyclic refinement of high intensity neutron powder-diffraction data was used to determine the temperature dependence of C1 and C2 and, thereby, of the moment orientation of each of the three Tb sites as well as of the unit-cell parameters. Figures 6(a) and 6(b) show that in Tb_3Ni_2 β and a increase below T_C, while b and c decrease. The nonsteady evolution with temperature of the magnetic moment components C1 and C2 shown in Figs. 6(c) and 6(d) does not have any incidence on the temperature-dependent behavior of the unit-cell parameters. The temperature evolutions of the magnetic moment directions on the three Tb sites are shown in Fig. 6(e). The magnetic moments of the sites Tb2 and even more strongly those on the site Tb3 are reorienting towards the a-axis direction below about 50 K (Tb2) and 70 K (Tb3) while the moment direction of the site Tb1 stays nearly constant below 70 K. These changes are, however, not responsible for the changes seen in the thermodiffractogram at about 80 K. The strong decrease of the (001) reflection

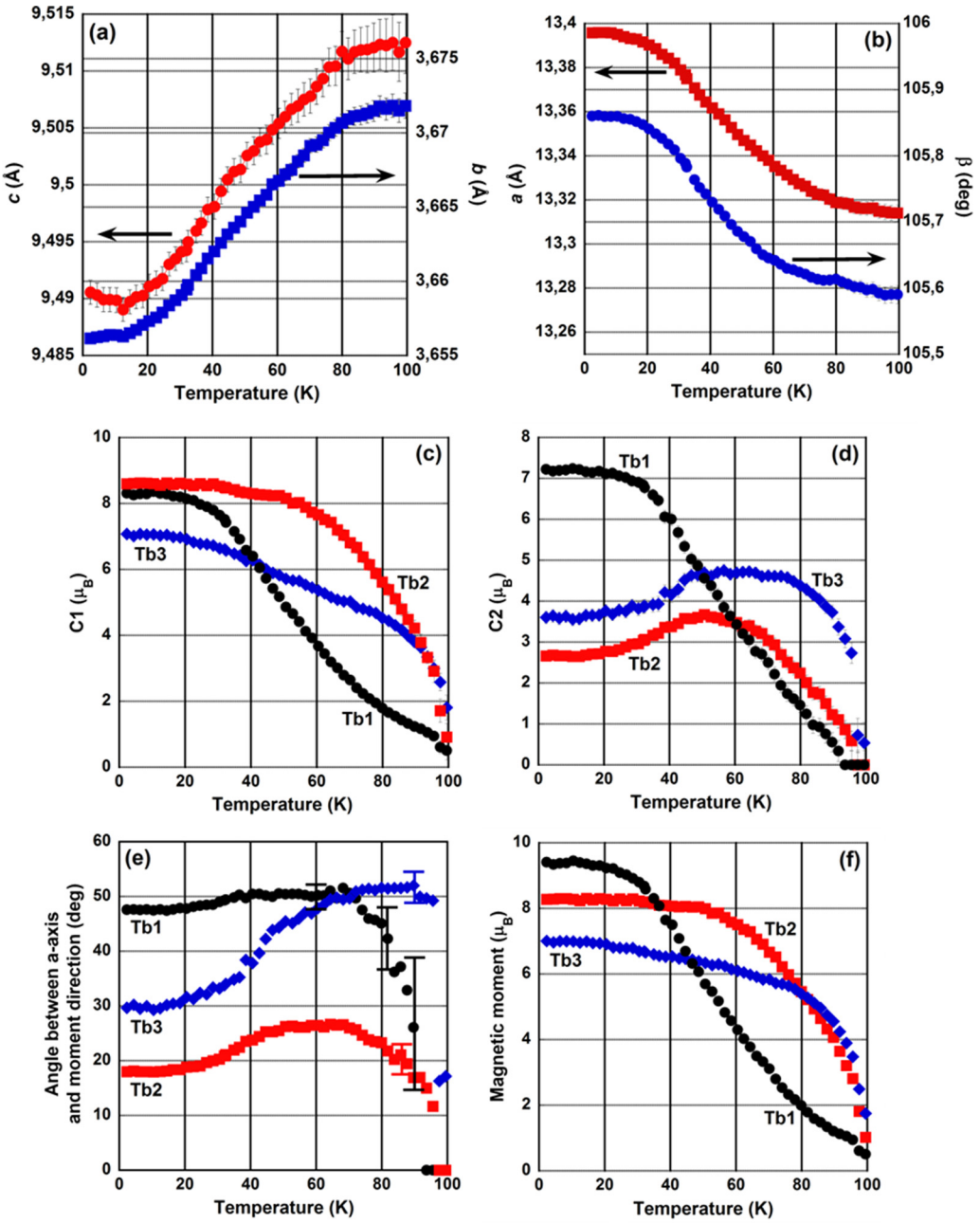

FIG. 6. Thermal dependence of the unit-cell parameters of Tb_3Ni_2 (a), (b), of the coefficients of the BVs for the three Tb sites (c), (d), and of their moment directions (e) and total values (f).

can instead be related to the strongly differing temperature dependence of the magnetic moment sizes of the three sites: Fig. 6(f) shows that the magnetic moment of the Tb1 site develops slowly below T_C and seems to be first induced by those of the Tb2 and Tb3 sites. The intensity of the 001 reflection is determined by the structure factors of the three sites with that of the Tb1 site having an opposite sign to those of the Tb2 and Tb3 sites, which leads to the 001 reflection going through a maximum before decreasing with increasing Tb1 moment size. The fact that the magnetic order on the Tb1 sublattice follows a different temperature dependence could be related to the more isolated situation and the strictly two-dimensional nature of this sublattice within the network of Tb-Tb bonds of the three-dimensional (3D) structure. The average bond lengths are very similar, however, while within the Tb1 sublattice five out of eight nearest-neighbor bonds are between Tb1 and only three bonds are connecting this sublattice to the Tb2/Tb3 network, the connectivity between the Tb2 and the Tb3 sublattices is very strong. The different temperature dependencies of the magnetic moment evolution on the three Tb sublattices [Figs. 6(c)–6(f)] together with the spin reorientation processes should be responsible for the unsteady behavior of the magnetization of Tb_3Ni_2 below T_C [Fig. 2(a)].

The temperature dependence of the unit-cell parameters of the $x(\mathrm{Co}) = 0.3$ compound as determined from the

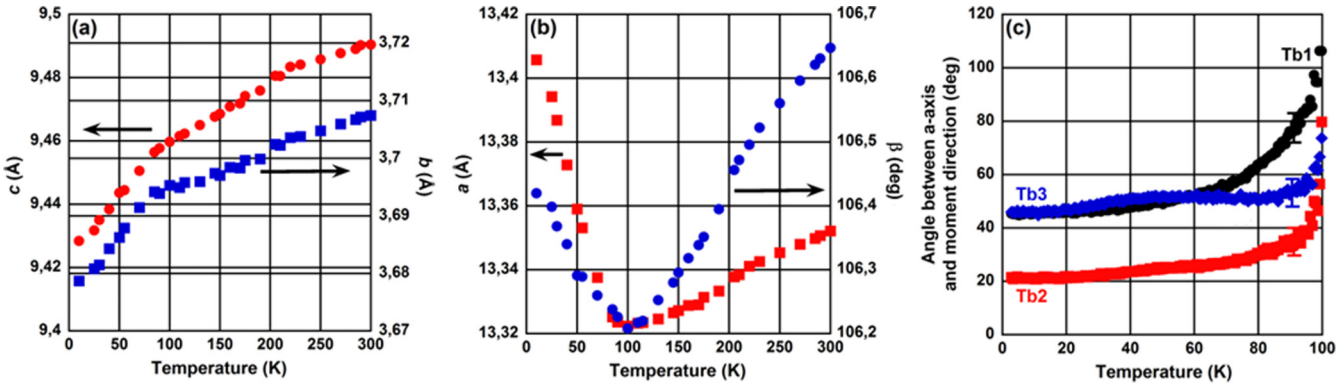

FIG. 7. Thermal dependence of the unit-cell parameters of $Tb_3Co_{0.3}Ni_{1.7}$ (a), (b) and temperature dependence of the individual magnetic moment directions of $Tb_3Co_{0.325}Ni_{1.675}$ (c). Error bars in (a) and (b) are smaller than the symbol size.

synchrotron data shows a behavior similar to Tb_3Ni_2 with b and c decreasing [Fig. 7(a)] and a and β increasing [Fig. 7(b)] below T_C. This compound and the 0.325 sample show as well a very similar behavior to the temperature dependence of the magnetic moments compared to Tb_3Ni_2, indicating that the magnetic interactions governing the appearance of the magnetic order remain nearly unperturbed by the exchange of Ni by Co. The only apparent difference when x increases from 0 to 0.325 is the order of the appearance of the two magnetic components in (100) and (001) directions. This is best seen when comparing Figs. 6(e) and 7(c) where the angle between the magnetic moment and the a-axis direction is drawn as a function of temperature. In Tb_3Ni_2 the magnetic moments are first aligned along the a axis corresponding to the C1 component whereas in $x = 0.325$ it is the C2 component along the c axis which appears first. The difference in the low-temperature orientation of the magnetic moments on the three Tb sites is, however, insignificant. As the total moment sizes do not vary as well (Table III) it can be concluded that the $C2/m$ structure seems to accommodate equally well the large magnetic moments along the range $0 \leqslant x \leqslant 0.325$; there is no reason to expect a magnetostructural transition on further doping with Co.

2. *Compositions* $0.35 \leqslant x(\mathrm{Co}) \leqslant 1$

Compounds within this region adopt at room temperature the rhombohedral Er_3Ni_2-type structure, space group $R\bar{3}h$, with Tb on Wyckoff positions $3a$, $6c$, and $18f$ and Co/Ni statistically distributed on the $18f$ site. Figure S6 in SM shows the Rietveld refinement of the room-temperature neutron-diffraction data of $Tb_3Co_{0.35}Ni_{1.65}$, and Table SIV in SM lists the results of the refinements together with those for $x = 0.5$ and 1.0 [17].

As in the range $0 \leqslant x \leqslant 0.325$ (Table II), the replacement of Ni by Co leads to a decrease of the unit-cell volume. In order to follow the volume effect on doping with Co over the whole range where different crystallographic symmetries exist, the quantity V_{at} which represents the volume of the unit cell divided by the number of atoms within the unit cell is introduced. Comparing the values of V_{at} given in Table II and in Tables SIII and SIV in SM [17], it can be seen that the shrinkage of V_{at} on cooling ($\Delta V_{\mathrm{at}} = -0.21$ Å^3 for, e.g., $x = 0.325$) is as pronounced as the shrinkage when x changes from 0 to 1 ($\Delta V_{\mathrm{at}} = -0.23$ Å^3). The volume per atom available at room temperature ($V_{\mathrm{at}} = 22.393$ Å^3) in $Tb_3Co_{0.35}Ni_{1.65}$, which is crystallizing in space group $R\bar{3}h$, is significantly larger than that of $Tb_3Co_{0.325}Ni_{1.65}$ at 1.5 K [$V_{\mathrm{at}} = 22.285$ Å^3 (Table II)], which still adopts the $C2/m$ symmetry. This result points to the fact that it cannot be solely the volume contraction induced by the substitution of Ni by Co which leads to the symmetry change from $C2/m$ to $R\bar{3}h$. Otherwise the volume contraction induced by cooling should have induced this symmetry change in $Tb_3Co_{0.325}Ni_{1.65}$. Similar magnetic phase transitions appear in all three compounds on cooling; Fig. 8(a) shows the thermodiffractogram of Tb_3CoNi. Fitting the integrated intensity of the strongest magnetic Bragg peaks, the magnetic transition temperatures were determined to be $T_C = 89$, 95, and 101 K for $x = 0.35$, 0.5, and 1, revealing a steady increase with increasing x(Co). Opposite to the situation in the compounds with $0 \leqslant x \leqslant 0.325$ [see Fig. 5(a)], the thermodiffractograms do not show any indication for a different temperature dependence of different magnetic sites.

From the position of the magnetic Bragg peaks the magnetic propagation vector is $\kappa = 0$. Magnetic symmetry analysis was used to determine the allowed IRs for the sites $3a$, $6c$, and $18f$ of space group $R\bar{3}h$. Trying to refine the high angular resolution diffraction data taken at 1.5 K it had to be realized that none of the allowed IRs is able to explain the measured magnetic intensities. The best refinement was achieved assuming a purely ferromagnetic-type structure with components in the directions of the a and the c vectors. This model, which does not represent an allowed IR, was able to account approximately for the magnetic intensities within the low angle region but failed completely to describe the diffracted intensities at 2Θ values above 50°. The high angle region of a neutron-diffraction pattern corresponding to the high-Q region is normally dominated by the nuclear scattering. In the here measured compounds the situation is, however, different as the only slowly falling magnetic form factor of the Tb^{3+} ion and its very large magnetic moment lead to a very strong magnetic contribution to the scattering at high-Q values. Although a structural transition was strongly assumed to be present in Tb_3CoNi it was not possible to use the low-temperature high angular resolution

TABLE III. Results of the Rietveld refinements of the low-temperature synchrotron (S) or high angular resolution neutron (N) powder-diffraction data of $Tb_3Co_xNi_{2-x}$ in space group $R\bar{1}$. Tb1 is on Wyckoff position 1*a*, and all other atoms are on 2*i*. V_{at} represents the volume per atom within the unit cell. Results of the magnetic structure refinement with use of the BVs 100, 010, and 001 pointing in the direction of the triclinic unit-cell directions are shown. μ_{Tb} represents the resulting total magnetic moment.

x, *T*	0.34 (N) 3.5 K	0.35 (N) 1.5 K	0.5 (N) 1.5 K	0.5 (S) 10 K	1 (N) 3.5 K	1 (S) 10 K
a (Å)	8.5855(2)	8.5927(3)	8.5915(2)	8.59795(4)	8.6067(4)	8.6072(1)
b (Å)	8.5213(2)	8.5232(2)	8.5296(2)	8.53573(4)	8.5592(3)	8.5617(1)
c (Å)	15.7227(4)	15.7171(4)	15.6967(3)	15.70689(7)	15.5966(6)	15.5986(1)
α (°)	89.957(2)	89.959(2)	90	89.9947(3)	90.069(4)	90.0531(5)
β (°)	90.949(2)	90.946(2)	90.907(2)	90.9175(3)	90.714(3)	90.6986(4)
γ (°)	119.816(2)	119.787(2)	119.788(2)	119.7964(2)	119.746(4)	119.7659(4)
V	997.83	998.83	998.12	1000.16	997.45	997.72
V_{at}	22.17	22.20	22.18	22.22	22.17	22.17
Tb2 *x*	0 fixed	0.9977(8)	0.0003(7)	0.0010(4)	0.9966(6)	0.0013(4)
y	0 fixed	0.997(1)	0.9967(8)	0.9986(5)	0.9957(9)	0.9997(6)
z	0.2088(1)	0.2093(1)	0.2091(1)	0.2090(2)	0.2115(2)	0.2106(2)
Tb3 *x*	0.0972(4)	0.0984(5)	0.0992(4)	0.0977(4)	0.0979(6)	0.0986(4)
y	0.4112(4)	0.4129(5)	0.4112(4)	0.4115(5)	0.4120(7)	0.4108(5)
z	0.0738(2)	0.0735(2)	0.0735(2)	0.0732(2)	0.0734(3)	0.0739(2)
Tb4 *x*	0.5881(4)	0.5863(5)	0.5880(4)	0.5880(4)	0.5894(6)	0.5877(4)
y	0.6857(4)	0.6848(5)	0.6849(4)	0.6859(5)	0.6899(8)	0.6883(5)
z	0.0734(2)	0.0718(2)	0.0732(2)	0.0729(2)	0.0721(3)	0.0728(2)
Tb5 *x*	0.3145(4)	0.3163(5)	0.3145(4)	0.3139(4)	0.3132(6)	0.3102(4)
y	0.9017(4)	0.9038(4)	0.9022(4)	0.9029(5)	0.9020(7)	0.9014(5)
z	0.0725(2)	0.0718(4)	0.0727(2)	0.0733(2)	0.0708(3)	0.0724(2)
Co1/Ni1 *x*	0.3121(4)	0.3123(7)	0.3141(6)	0.311(1)	0.311(2)	0.317(1)
y	0.2480(6)	0.2479(8)	0.2495(6)	0.251(1)	0.252(2)	0.255(1)
z	0.1015(3)	0.1041(4)	0.1031(3)	0.1039(5)	0.1050(6)	0.1024(5)
Co2/Ni2 *x*	0.7495(6)	0.7513(8)	0.7519(6)	0.751(1)	0.745(1)	0.753(1)
y	0.0633(6)	0.0636(8)	0.0644(6)	0.065(1)	0.059(1)	0.064(1)
z	0.1025(3)	0.1046(4)	0.1037(3)	0.1029(5)	0.1063(6)	0.1052(5)
Co3/Ni3 *x*	0.9361(6)	0.9375(7)	0.9389(6)	0.936(1)	0.939(1)	0.939(1)
y	0.6888(6)	0.6895(7)	0.6916(6)	0.686(1)	0.686(1)	0.688(1)
z	0.1036(3)	0.1035(3)	0.1029(3)	0.1028	0.1055(6)	0.1037(6)
R_{Bragg}	2.8	3.6	3.2	4.1	4.7	6.8
Tb1 100	9.2(2)	10.0 (2)	10.2(2)		9.2(2)	
010	5.8(3)	6.3(3)	6.8(3)		5.8(4)	
001	–2.3(1)	–1.3(2)	–1.9(2)		–1.3(2)	
$\mu_{Tb1}(\mu_B)$	8.4(3)	9.0(3)	9.3(3)		8.2(4)	
Tb2 100	10.2(1)	10.6(2)	10.5(2)		10.0(2)	
010	4.4(2)	4.8(3)	4.9(3)		5.0(3)	
001	–1.6(1)	–1.7(2)	–1.4(1)		–0.9(2)	
$\mu_{Tb2}(\mu_B)$	9.1(2)	9.4(3)	9.3(3)		8.8(4)	
Tb3 100	6.8(2)	8.1(2)	7.9(2)		8.3(2)	
010	1.8(2)	1.7(3)	2.5(2)		3.0(2)	
001	–6.0(2)	–5.3(2)	–6.1(2)		–4.4(3)	
$\mu_{Tb3}(\mu_B)$	8.6(3)	9.2(3)	9.4(3)		8.7(4)	
Tb4 100	6.2(2)	6.6(2)	7.0(3)		6.4(3)	
010	5.6(2)	5.2(3)	7.0(3)		7.3(3)	
001	–7.3(2)	–6.4(3)	–7.2(3)		–6.8(3)	
$\mu_{Tb4}(\mu_B)$	9.4(3)	8.9(3)	10.1(4)		9.8(4)	
Tb5 100	6.7(2)	7.1(2)	7.4(2)		8.7(2)	
010	3.1(3)	2.9(3)	3.8(3)		4.1(3)	
001	–7.4(2)	–7.6(2)	–7.1(3)		–6.0(2)	
$\mu_{Tb5}(\mu_B)$	9.4(3)	9.9(3)	9.7(4)		9.8(4)	
R_{Mag}	2.0	2.5	2.2		3.5	

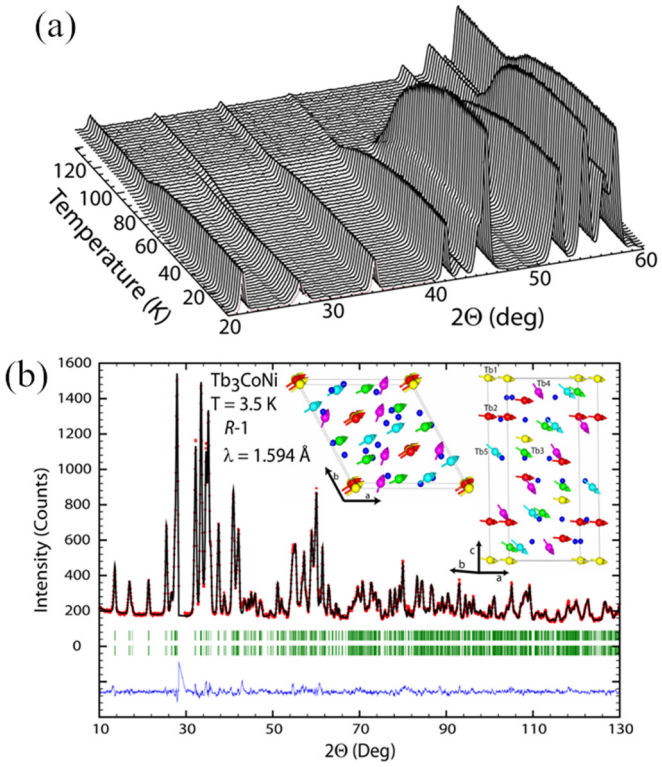

FIG. 8. (a) Low 2Θ part of the thermal dependence of the neutron-diffraction pattern of Tb_3CoNi. (b) Rietveld refinement of the high angular resolution neutron powder data of Tb_3CoNi at 3.5 K in the space group $R\bar{1}$. Observed (dots, red), calculated (black, line), and difference patterns are shown. The tick marks indicate the calculated positions of the nuclear Bragg peaks. The insets show the magnetic structure, and blue balls represent the transition-metal (Co/Ni) sites.

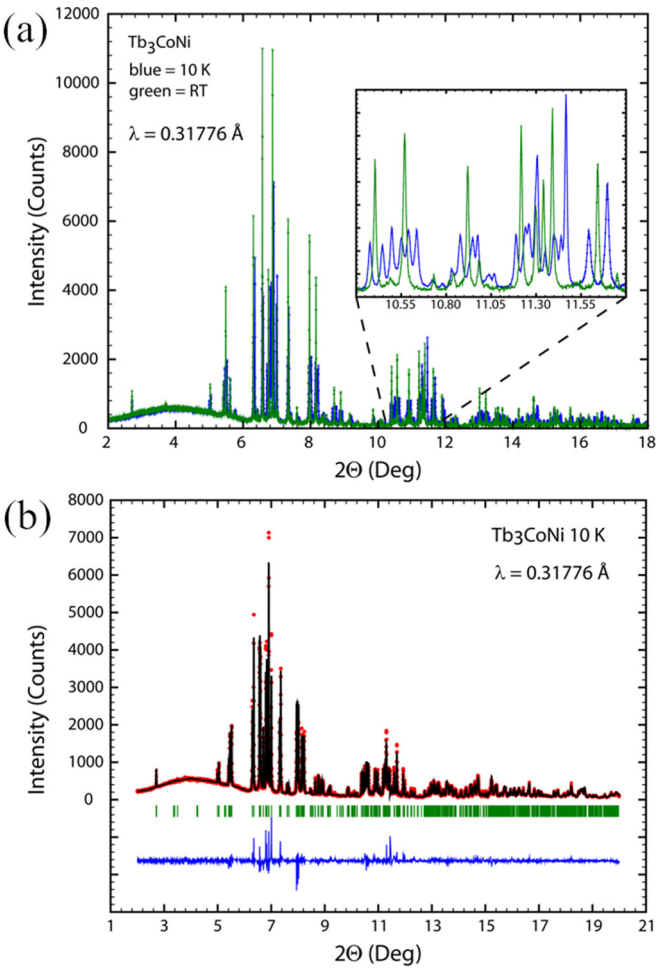

FIG. 9. (a) Synchrotron data of Tb_3CoNi at room temperature and 10 K showing a strong structural distortion at low temperatures. (b) Rietveld refinement of the synchrotron powder data of Tb_3CoNi at 10 K in the space group $R\bar{1}$. Observed (dots, red), calculated (black, line), and difference patterns are shown. The tick marks indicate the calculated position of the Bragg peaks.

neutron diffraction to determine the symmetry of the new structure.

Synchrotron measurements on Tb_3CoNi were therefore performed at several temperatures; Fig. 9 shows data taken at room temperature and at 10 K. The comparison of the two data sets reveals that the symmetry of the crystallographic structure of Tb_3CoNi is strongly reduced at low temperatures. LeBail refinements of the 10-K data show that only a triclinic symmetry is able to account for the diffraction pattern. A symmetry reduction to space group $P\bar{1}$ leads to an increase of independent atom positions from 4 in $R\bar{3}h$ to 22 in $P\bar{1}$ and of the adjustable positional parameters from 7 to 63. Assuming, however, that the R centering is kept through the structural transition, a refinement in the nonstandard setting $R\bar{1}$ reduces the number of atom positions to 8 and of positional parameters to 21. While the $3a$ and $6c$ sites of Tb in $R\bar{3}h$ keep their multiplicities the $18f$ sites splits into three sixfold sites each in $R\bar{1}$. This leads to five different Tb positions and three different transition-metal sites (also see Table III). Using this constraint a stable refinement of the synchrotron data of Tb_3CoNi at 10 K (Fig. 9) was possible and returned unit-cell parameters of $a = 8.6072(1)$ Å, $b = 8.5617(1)$ Å, $c = 15.5986(1)$ Å, $\alpha = 90.0531(5)^\circ$, $\beta = 90.6986(4)^\circ$, and $\gamma = 119.7659(4)^\circ$.

Knowing the type of structural distortion the analysis of the low-temperature neutron data becomes straightforward. Magnetic symmetry analysis of the two different Tb positions on 0,0,0 (Wyckoff site $1a$ in $P\bar{1}$) and x, y, z (Wyckoff site $2i$ in $P\bar{1}$) shows that the twofold site can see either a FM or an antiferromagnetic coupling of the symmetry related sites with BVs pointing in the three unit-cell directions. Assuming that the R centering remains present at low temperature as well for the magnetic structure this limits the number of possible magnetic structures strongly even though the independent Tb sites may follow different BVs. Testing the different solutions against the measured neutron data, only the purely ferromagnetic structure is able to explain the pattern. Including magnetic moments on the three transition-metal sites the R factors of the refinements are getting only marginally smaller with values of about 1–2 μ_B per site. Compared to the strong magnetic contribution from the Tb sublattices this would – if real – represent less than 3% of the total magnetic scattering. It is not possible to exclude the possibility of having small

magnetic moments on these sites but they are not needed for achieving a very good refinement.

The resulting fit of the high angular resolution powder-diffraction data measured at 3.5 K assuming magnetic moments only on the Tb sites is shown in Fig. 8(b) with the adopted magnetic structure displayed in the inset. Table III lists the structural and magnetic details of this refinement. Whereas the magnetic moments of Tb1, Tb2, Tb3, and Tb5 are pointing nearly in the same direction within the *a*-*b* plane, Tb4 is inclined by about 45° to their direction. While the collinearity of Tb1 and Tb2 is nearly perfect, the magnetic moments of sites Tb3–Tb5 see an additional significant component along the *c* direction. Due to the insufficient resolution of the high intensity data it was not possible to study the temperature dependence of the individual magnetic moments of the five Tb sites as it had been done for Tb_3Ni_2 (see above). However, the refinement of the seven high angular resolution neutron patterns between 3.5 and 79 K allowed concluding that the five Tb sites in the $R\bar{1}$ phase of Tb_3CoNi are all showing similar temperature dependence. These refinements indicated as well a strong correlation between the appearance of the triclinic distortion and that of the ordered magnetic moments, a point which will be studied in more detail below using data on $Tb_3Co_{0.5}Ni_{1.5}$.

The magnetization data $M(H)$ of the $x = 0.5$ and 1 compounds found values of $M_S = 7.89\,\mu_B$/Tb at $T = 2$ K and $M_S = 7.30\,\mu_B$/Tb at $T = 4$ K, respectively, for the saturation magnetizations (Fig. 3). Using the values of the magnetic moments as determined from the neutron-diffraction data listed in Table III one would obtain values of $9.6\,\mu_B$/Tb ($x = 0.5$) and $9.1\,\mu_B$/Tb ($x = 1$). If, however, only the in-plane parts (along 100 and 010) of the magnetic moments are taken into account the corresponding average magnetic moment would amount to about $7.8\,\mu_B$/Tb for both compounds, close to the obtained value from the $M(H)$ data. This could indicate that the magnetic fields employed in the magnetization measurements were not sufficient to reorient the out-of-plane component of the magnetic moments. The thermodiffractograms of the compounds with $x = 0.35$ and 0.5 show a very similar behavior to Tb_3CoNi. Using the high angular resolution neutron powder data the same structural transition to a triclinic structure and the same magnetic structures were found. Details of the results of the low-temperature refinements are included in Table III. The distortion to $R\bar{1}$ is most strongly reflected in the change of the unit-cell parameters while the atom coordinates vary little or not at all from the position they occupy within the $R\bar{3}h$ phase. Table III shows that the structural distortion leads to differences of 0.8–0.5% between the *a* and *b* lattice parameters at the lowest temperature. While the unit-cell angle α stays close to 90°, γ deviates clearly from 120° and β deviates even more strongly from 90°. The relative stability of the atom positions is best seen when comparing the atom positions of Tb2 in the original $R\bar{3}h$ symmetry with the one adopted in $R\bar{1}$: located on position 6*c* (0,0,*z*) in $R\bar{3}h$, the coordinates of the new site 2*i* (*x*, *y*, *z*) in $R\bar{1}$ only marginally deviate from zero for the *x* and *y* parameters as they refine to $x = 0.997$–0.001 and $y = 0.996$–0.000 for the $x = 0.35$, 0.5, and 1 compounds (Table III). Similar small differences can be found when comparing the adopted positions of the Tb3, Tb4, and Tb5 sites in $R\bar{1}$ which were linked through the symmetry operators of Wyckoff site 18*f* in $R\bar{3}h$. This fact comforts our decision to refine the low-temperature data of the compounds undergoing the structural transition in the nonstandard space group $R\bar{1}$ and not in $P\bar{1}$ with the same pseudorhombohedral unit cell where the number of independent positional parameters would have been even larger. Indeed, it is possible to select a standard $P\bar{1}$ unit cell with three times smaller volume, but such transformation will not be as intuitive in demonstrating the intimate relationship between the high-temperature rhombohedral and the low-temperature triclinic unit cells.

The temperature dependence of the structure and of the triclinic distortion of the compound $Tb_3Co_{0.5}Ni_{1.5}$ was studied in more detail with the use of synchrotron radiation data. Figure S7 in SM [17] displays the results for the lattice parameters: while at 100 K the data can be refined nearly perfectly within space group $R\bar{3}h$, data at 80 K and below show the triclinic distortion. This distortion can be quantified by the difference between the *a*- and *b*-unit-cell parameters and by the deviation of the angles from the ideal hexagonal values. The *a* and *b* parameters diverge and the triclinic angles β and γ deviate, respectively, from 90° and 120° with decreasing temperature. This trend seems to be still strong at base temperature although the increase of the magnetic moments has come to an arrest at about 30 K. No significant cell volume change occurs at T_C but the volume continues to decrease even below 50 K where the phonon contributions should be nearly constant.

From Fig. S7 in SM [17] it becomes clear that $Tb_3Co_{0.5}Ni_{1.5}$ sees a strong anisotropic spontaneous magnetostriction below T_C. The magnetic structure is such [insets of Fig. 8(b)] that the direction of the resulting magnetization of the Tb sublattices does not point in direction of the hexagonal *c* axis. Relative to the hexagonal symmetry the direction of the ferromagnetic alignment of the sublattices is arbitrary, breaking it thereby totally through the effect of the strong single ion anisotropy of the Tb^{3+} ions. The resulting magnetic space group is $P\bar{1}$ (2.4).

3. *Composition* x(Co) = 0.34

In the quest for a composition where the structural transition from *C*2/*m* to $R\bar{3}h$ could take place as a function of temperature the compound $Tb_3Co_{0.34}Ni_{1.66}$ was synthesized knowing that the compound with $x = 0.325$ adopts still the *C*2/*m* structure while $x = 0.35$ is already $R{-}3h$. A first refinement of high angular resolution neutron powder data taken at room temperature worked satisfactorily assuming for the structure the space group $R\bar{3}h$; however, the presence of weak peaks not accounted for in this space group indicated the possible presence of a second phase. Low-temperature data taken at 3.5 K revealed furthermore the appearance of magnetic Bragg peaks which were as well not accounted for by the magnetic structure formerly found for the phases with $0.35 \leqslant x \leqslant 1$. As the position of these additional magnetic peaks corresponds to those of the magnetic *C*2/*m* phase, a new refinement assuming the coexistence of two structurally different phases was attempted. Figure S8(a) in SM [17]

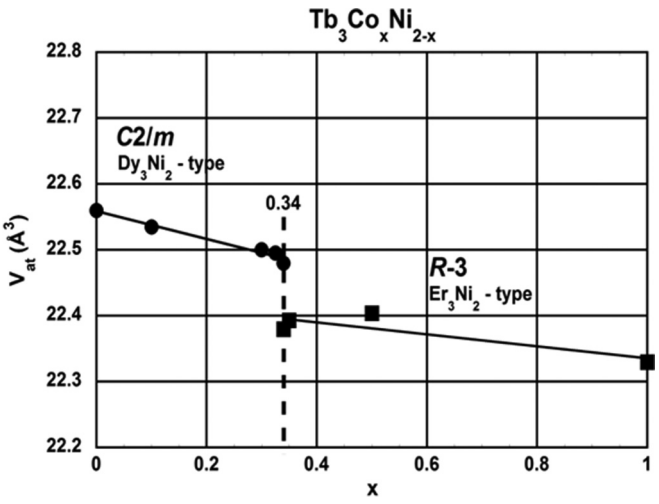

FIG. 10. Phase diagram at room temperature of the pseudobinary system $Tb_3Co_xNi_{2-x}$. At $x = 0.34$ coexistence of 8.5% $C2/m$ and 91.5% $R\bar{3}h$ phases is shown.

displays this two-phase refinement where a coexistence of about 91.5% $R\bar{3}h$ with 8.5% $C2/m$ phases was determined, improving significantly the goodness of the fit from $\chi^2 = 7$ for the single phase to $\chi^2 = 3$ for the two-phase material.

The coexistence of two structural phases at room temperature indicated that the chosen composition with $x = 0.34$ was ideally placed to verify the possibility of a structural transition from $R\bar{3}h$ to $C2/m$ or vice versa as a function of decreasing temperature. Surprisingly, however, the high angular resolution neutron data taken at 3.5 K [see Fig. S8(b) in SM [17]] show that the concentrations of phases do not change between the two structures upon lowering the temperature. The only constraint applied for this refinement was the fixing of the atom coordinates of the minority phase $C2/m$ to the values found for the $x = 0.325$ compound. While the refinement leads to phase concentrations of 91.6(0.8) to 8.4(0.2)% at room temperature the data at 3.5 K show the ratio of 91.4(1.3) to 8.6(0.3)%. The magnetic structures adopted by the two nuclear phases correspond to those already found in the corresponding single-phase regions. The results of these refinements are included in Table III and in Tables SIII and SIV in SM [17].

D. Phase diagram

The results of the temperature-dependent neutron and synchrotron measurements allow drawing the phase diagram of the pseudobinary system $Tb_3Co_xNi_{2-x}$. Figure 10 displays the change from the monoclinic Dy_3Ni_2-type structure ($C2/m$) to the rhombohedral Er_3Ni_2-type ($R\bar{3}h$) structure as function of composition. The transition between the two structure types is situated at about $x = 0.34$ and englobes a small region of coexistence. No trace of an intermediate structure of Y_3Co_2 type has been found. Doping with Co induces shrinkage of the unit-cell volume and the volume occupied per atom V_{at} jumps to a smaller value as the system changes from the Dy_3Ni_2 type to the Er_3Ni_2 type. However, even in the very narrow range of concentrations where two phases coexist, a transition between the two structure types cannot be induced by a change in temperature.

III. SUMMARY AND CONCLUSIONS

At low temperatures a transition to a ferromagnetically ordered state takes place for all compounds of this pseudobinary system. The magnetic transition within the region of compounds adopting the $C2/m$ symmetry is independent of the value of x(Co) and occurs at $T_C \approx 100$ K. The three Tb sublattices adopt a nearly collinear magnetic structure within the monoclinic a-c plane with the magnetic space group $C2'/m'$. The magnetic order on one of the three Tb sites seems to be induced by the presence of magnetic order on the other two sublattices which can be tentatively explained by the more isolated situation of this sublattice within the 3D structure. The presence of three Tb sublattices possessing different T dependencies combined with a continuous change of the magnetic moment directions of these three sublattices is reflected in the atypical behavior of the magnetization data of Tb_3Ni_2 which recalls an antiferromagnetic compound.

Compounds with $x(\text{Co}) \geqslant 0.34$ undergo a structural transition from $R\bar{3}h$ to triclinic ($R\bar{1}$, nonconventional setting) at the magnetic ordering temperature which increases from $T_C = 89$ K for $x = 0.35$ to $T_C = 101$ K for $x = 1$. The concomitance of magnetic and structural transitions explains the presence of a much stronger anomaly in the heat capacity of Tb_3CoNi when compared to Tb_3Ni_2 which does not see a structural transition. The strong triclinic distortion leads in Tb_3CoNi at the lowest temperatures to a difference of 0.5–0.8% between the originally equal a- and b-unit-cell parameters and can be linked to the anisotropic spontaneous magnetostriction exerted by the symmetry-breaking ferromagnetic alignment of the five Tb sublattices (magnetic space group $P\bar{1}$) which does not conform to the original hexagonal symmetry and is furthermore not collinear. No sign of a magnetic moment could be detected on the transition-metal sites for any of the compounds. The existence of a structural transition linked to the appearance of magnetic long-range order has been noted before in different compounds such as, e.g., CeScSi [26], $CuCrS_2$ [27], $Gd_5Si_2Ge_2$ [28], $ErAl_2$ [29], and Eu_2In [30] but still remains a rarely found phenomenon. This fact can probably be explained by an insufficient search for structural details at low temperatures—a situation which began to change with the increasing use of standard laboratory powder diffractometers and availability synchrotron facilities, both employing He cryostats, allowing data to be taken down to temperatures where rare-earth magnetism prevails or frustrated systems order.

Data from ILL is available [31].

ACKNOWLEDGMENTS

The authors would like to acknowledge ILL for beam time allocation experiment code 5-31-2407. Work at Ames Laboratory is supported by the U.S. Department of Energy, Office of Science, Basic Energy Sciences, Materials Sciences and Engineering Division. The Ames Laboratory is operated for the U.S. Department of Energy by Iowa State University of Science and Technology under Contract No. DE-AC02-07CH11358.

[1] *Rare Earths, Science, Technology, Production and Use*, edited by J. Lucas, P. Lucas, T. Le Mercier, A. Rollat, and W. Davenport, 1st ed. (Elsevier, New York, 2015).

[2] *Rare Earths Industry, Technological, Economic, and Environmental Implications*, edited by I. Borges De Lima and W. Leal Filho (Elsevier, New York, 2015).

[3] K. Zhang, A. N. Kleit, and A. Nieto, Renew. Sust. Energy Rev. **77**, 899 (2017).

[4] P. Manfrinetti, A. Provino, and K. A. Gschneidner, Jr., J. Alloys Compd. **482**, 81 (2009).

[5] C. Ritter, S. K. Dhar, R. Kulkarni, A. Provino, D. Paudyal, P. Manfrinetti, and K. A. Gschneidner, Jr., J. Phys.: Condens. Matter **26**, 366001 (2014).

[6] A. Provino, P. Manfrinetti, K. A. Gschneidner, Jr., S. K. Dhar, D. L. Schlagel, T. A. Lograsso, G. J. Miller, S. Thimmaiah, H. Wang, A. M. Russell, A. Becker, and Y. Mudryk, Acta Mater. **73**, 27 (2014).

[7] A. Provino, K. A. Gschneidner, Jr., S. K. Dhar, C. Ferdeghini, Y. Mudryk, P. Manfrinetti, D. Paudyal, and V. K. Pecharsky, Acta Mater. **91**, 128 (2015).

[8] T. B. Massalski, *Binary Alloy Phase Diagrams*, 2nd ed. (ASM, Metals Park, OH, 1990).

[9] P. Villars and K. Cenzual, *Pearson's Crystal Data - Crystal Structure Database for Inorganic Compounds (on DVD), Release 2017/18* (ASM International, Materials Park, OH, 2017).

[10] J. M. Moreau, D. Paccard, and E. Parthé, Acta Crystallogr. B **30**, 2583 (1974).

[11] J. M. Moreau, D. Paccard, and D. Gignoux, Acta Crystallogr. B **30**, 2122 (1974).

[12] J. Le Roy, J. M. Moreau, D. Paccard, and E. Parthé, Acta Crystallogr. B **33**, 3406 (1977).

[13] G. Xu, Y.-W. Cui, H. Fei, L. Zhang, F. Zheng, L. Liu, and Z. Jin, Int. J. Mater. Res. **103**, 1179 (2012).

[14] A. Provino, P. Manfrinetti, M. Putti, D. Paudyal, and K. A. Gschneidner, Jr., Proceedings of the American Physical Society 2014 Conference, 2014.

[15] A. Provino, V. Smetana, D. Paudyal, K. A. Gschneidner, Jr, A.-V. Mudring, V. K. Pecharsky, P. Manfrinetti, and M. Putti, J. Mater. Chem. C **4**, 6078 (2016).

[16] Q. Y. Dong, J. Chen, J. Shen, J. R. Sun, and B. G. Shen, Appl. Phys. Lett. **99**, 132504 (2011).

[17] See Supplemental Material at http://link.aps.org/supplemental/10.1103/PhysRevMaterials.3.024406 for experimental methods; SEM microphotographs of $Tb_3Co_xNi_{2-x}$ samples; sketches of the monoclinic Dy_3Ni_2 type and rhombohedral Er_3Ni_2 type; inverse magnetic susceptibility data of Tb_3Ni_2, $Tb_3Co_{0.5}Ni_{1.5}$, and Tb_3CoNi compounds; heat-capacity data of Tb_3Ni_2 and Tb_3CoNi; Rietveld refinement of the room-temperature synchrotron powder data of $Tb_3Co_{0.3}Ni_{1.7}$; Rietveld refinement of the room-temperature high angular resolution neutron-diffraction data of $Tb_3Co_{0.35}Ni_{1.65}$; thermal dependence of the unit-cell parameters of $Tb_3Co_{0.5}Ni_{1.5}$ in both the rhombohedral $R\bar{3}h$ and triclinic distortion $R\bar{1}$ space groups; Rietveld refinement of the high angular resolution neutron powder data of $Tb_3Co_{0.34}Ni_{1.66}$; lattice parameters and cell volumes of the $Tb_3Co_xNi_{2-x}$ compounds crystallizing in the Dy_3Ni_2 and Er_3Ni_2 types; Rietveld refinement data of the synchrotron (S) or high angular resolution neutron (N) powder-diffraction data at room temperature for $Tb_3Co_xNi_{2-x}$ in the space group $C2/m$; basis vectors of the allowed irreducible representations for $\kappa = 0$ for the Wyckoff position $4i$ of space group $C2/m$; and Rietveld refinement data of the synchrotron (S) or high angular resolution neutron (N) powder-diffraction data at room temperature for $Tb_3Co_xNi_{2-x}$ in space group $R\bar{3}h$.

[18] Q. Yao, Y. Wang, and H. Zhou, J. Alloys Compd. **395**, 98 (2005).

[19] *Alloy Phase Diagrams*, online ed. (ASM International, Metals Park, OH, 2006).

[20] P. Villars and J. L. C. Daams, J. Alloy Compd. **197**, 177 (1993).

[21] W. B. Pearson, *The Crystal Chemistry and Physics of Metals and Alloys* (Wiley-Interscience, New York, 1972).

[22] *Handbook on the Physics and Chemistry of Rare Earths*, edited by K. A. Gschneidner, Jr. and L. Eyring (North-Holland, Amsterdam, 1978), Vol. 1.

[23] V. K. Pecharsky and K. A. Gschneidner, Jr., Phys. Rev. Lett. **78**, 4494 (1997).

[24] L. Morellón, C. Magén, P. A. Algarabel, M. R. Ibarra, and C. Ritter, Appl. Phys. Lett. **79**, 1318 (2001).

[25] C. Ritter, A. Provino, P. Manfrinetti, V. K. Pecharsky, K. A. Gschneidner, Jr., and S. K. Dhar, J. Phys.: Condens. Matter **27**, 476001 (2015).

[26] C. Ritter, A. Provino, P. Manfrinetti, and A. K. Pathak, J. Phys.: Condens. Matter **29**, 045802 (2017).

[27] J. C. E. Rasch, M. Boehm, C. Ritter, H. Mutka, J. Schefer, L. Keller, G. M. Abramova, A. Cervellino, and J. F. Löffler, Phys. Rev. B **80**, 104431 (2009).

[28] Y. Mudryk, V. K. Pecharsky, and K. A. Gschneidner, Jr., in *Handbook on the Physics and Chemistry of Rare Earths*, edited by J.-C. Bunzli and V. K. Pecharsky (Elsevier, New York, 2014), Vol. 44, pp. 283–449.

[29] A. K. Pathak, D. Paudyal, Y. Mudryk, K. A. Gschneidner, Jr., and V. K. Pecharsky, Phys. Rev. B **94**, 224406 (2016).

[30] F. Guillou, A. K. Pathak, D. Paudyal, Y. Mudryk, F. Wilhelm, A. Rogalev, and V. K. Pecharsky, Nat. Commun. **9**, 2925 (2018).

[31] DOI: 105291/ILL-DATA.5-31-2407